THE JOURNAL OF PHYSICAL CHEMISTRY C

Article

pubs.acs.org/JPCC

# Water-Gas Shift and Methane Reactivity on Reducible Perovskite-Type Oxides

Ramona Thalinger,[†] Alexander K. Opitz,[‡] Sandra Kogler,[‡] Marc Heggen,[§] Daniel Stroppa,[∥] Daniela Schmidmair,[⊥] Ralf Tappert,[⊥] Jürgen Fleig,[‡] Bernhard Klötzer,[†] and Simon Penner*[,†]

[†]Institute of Physical Chemistry, University of Innsbruck, Innrain 80-82, A-6020 Innsbruck, Austria

[‡]Institute of Materials Chemistry, Vienna University of Technology, Getreidemarkt 9/BC/01 A-1060 Vienna, Austria

[§]Ernst Ruska Zentrum und Peter Grünberg Institut, Forschungszentrum Jülich GmbH, 52425 Jülich, Germany

[∥]International Iberian Nanotechnology Laboratory, Av. Mestre Jose Veiga s/n, 4715-330 Braga, Portugal

[⊥]Institute of Mineralogy and Petrography, University of Innsbruck, Innrain 52d, A-6020 Innsbruck, Austria

Supporting Information

**ABSTRACT:** Comparative (electro)catalytic, structural, and spectroscopic studies in hydrogen electro-oxidation, the (inverse) water-gas shift reaction, and methane conversion on two representative mixed ionic−electronic conducting perovskite-type materials $La_{0.6}Sr_{0.4}FeO_{3-\delta}$ (LSF) and $SrTi_{0.7}Fe_{0.3}O_{3-\delta}$ (STF) were performed with the aim of eventually correlating (electro)catalytic activity and associated structural changes and to highlight intrinsic reactivity characteristics as a function of the reduction state. Starting from a strongly prereduced (vacancy-rich) initial state, only (inverse) water-gas shift activity has been observed on both materials beyond ca. 450 °C but no catalytic methane reforming or methane decomposition reactivity up to 600 °C. In contrast, when starting from the fully oxidized state, total methane oxidation to $CO_2$ was observed on both materials. The catalytic performance of both perovskite-type oxides is thus strongly dependent on the degree/depth of reduction, on the associated reactivity of the remaining lattice oxygen, and on the reduction-induced oxygen vacancies. The latter are clearly more reactive toward water on LSF, and this higher reactivity is linked to the superior electrocatalytic performance of LSF in hydrogen oxidation. Combined electron microscopy, X-ray diffraction, and Raman measurements in turn also revealed altered surface and bulk structures and reactivities.

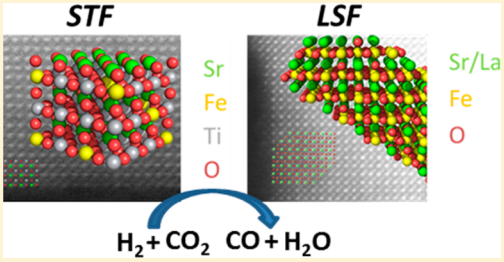


## 1. INTRODUCTION

A current trend in catalysis sees a refocus on the catalytic action of the individual parts of a more complex catalyst entity. As many catalyst systems represent a combination of (noble) metals and (oxidic) supporting materials, the latter are increasingly studied with respect to their intrinsic surface reactivity.[1−3] However, due to the inherent structural and electronic complexity of oxides, the identification of e.g. a "single" catalytically active site is far from being straightforward. This complexity is multiplied if more complex oxide systems are studied.[4] Such complex systems may either be two-phase systems such as mechanically mixed oxide powders[5,6](e.g., being promising methanol-to-gasoline catalysts[7]) or single-phase binary oxides adopting a distinct crystallographic structure.[8−10] A well-known example of the latter are perovskite-type materials with the general formula $ABO_3$, where A and B are cationic metal species with variable composition.[11] Their use as ferroelectrica,[12] high-temperature superconductors,[13] or solid oxide fuel cell (SOFC) cathodes[14] is already well-known. Potential applications in catalysis are reported for environmentally relevant de$NO_x$ processes, diesel exhaust catalysis, polymerization of olefins, total oxidation of hydrocarbons, or dry reforming of methane.[15−26] Specifically, also the water-gas shift reactivity has recently been in the focus of research.[27−29] A comprehensive review of the salient aspects of the structure and known catalytic performance of perovskites has been given by e.g. by Pena et al. or Royer et al.[30,31]

A rather new field of catalytic research deals with the replacement of the nowadays common Ni/YSZ SOFC anodes by acceptor-doped mixed conducting perovskite-type anodes.[32−35] For this application a combination of good ionic and electronic conductivity,[36] as well as high (electro)catalytic activity and high resilience against carbon deposition, is necessary. Acceptor-doped oxides under reducing conditions, however, often exhibit a relatively high ionic conductivity, but their rather low electronic conductivity may be problematic for an application as SOFC anode materials.[37−39] In the case of model-type thin film electrodes, this poor electronic conductivity can lead to an electronic sheet resistance and thus to inhomogeneous electrochemical polarization.[40,41] To avoid artifacts in electrochemical measurements, metallic thin film current collectors can be applied on such thin film electro-

Received: March 27, 2015
Revised: April 30, 2015
Published: May 4, 2015

  

DOI: 10.1021/acs.jpcc.5b02947
J. Phys. Chem. C 2015, 119, 11739−11753

des,[42,43] where the electrochemical surface activity of perovskite-type electrode materials can be separated from resistances due to poor current collection. Moreover, catalytic activity in carbon-based fuel reforming and hydrogen oxidation on Ni/YSZ electrodes is provided by the Ni phase. However, also perovskite-type lanthanum chromite/ferrite-based SOFC anodes have been shown to exhibit good catalytic activity for methane steam reforming and methane oxidation.[35] The understanding of the surface catalytic properties of such acceptor-doped perovskites in reducing atmospheres, however, is still in its infancy. With respect to fuel cell research and oxide surface chemistry, investigations on water-gas shift reactivity and hydrocarbon reforming are hence an obvious research field.[44−47]

The water-gas shift reaction is known to be catalyzed by redox-active oxidic materials, in particular also by more complex mixed systems such as $CuO/ZnO/Al_2O_3$, $Fe_2O_3/Cr_2O_3$,[48,49] or even perovskite materials.[50−53] Although there appears to be increasing interest in the general use of perovskite materials as valuable catalysts, also including hydrocarbon conversion reactions,[54−59] direct correlations of catalytic properties and associated structural changes for eventual determination of the catalytically active site still remain scarce due to the inherent complexity of these materials. This is a particular pity since e.g. hydrocarbon conversion is usually carried out at very high temperatures ($T$ > 600 °C), which might give rise to an array of structural changes, including (but not limited to) surface reconstruction, altering bulk and/or surface terminations, and/or chemical segregation of individual atom species. Especially the surface structure and chemistry, e.g., the cation concentration or the formation and amount of oxygen vacancies, are in a dynamical state depending on the experimental conditions.[60−63] For oxide and SOFC-related research this basically refers to the hydroxylation degree of the surface, high temperatures, and the oxygen partial pressure and reactivity. Thus, surface and bulk structure and composition might significantly deviate from one another and need to be separately assessed. Regarding chemical alterations of perovskite-type materials, cation segregation is already a well-known phenomenon especially under operational conditions of an SOFC.[64−69] Moreover, reversible *in situ* segregation of electrolysis-promoting metallic Fe species under reducing (cathodic) conditions was recently reported[70] as well as growth of defined nanoparticles by controlled perovskite nonstoichiometry.[71]

In order to fill this knowledge gap and to bridge the gap between SOFC-relevant reactivity and "conventional" catalysis, which also includes a cross-correlation between catalytic application and electrocatalysis, the present contribution aims at (i) characterizing the electrochemical surface activity of perovskite-type materials (in particular LSF) in both oxidizing and reducing atmosphere by means of impedance spectroscopy. To account for the low electronic conductivity of acceptor-doped mixed conductors in reducing atmosphere (see above), model-type thin film electrodes with a current-collecting platinum thin film grid are used in these investigations. (ii) As the specific oxygen reactivity is suspected to play a major role in eventually steering the catalytic reactivity, the main goal of this study is to highlight reactivity differences for the (inverse) water-gas shift ((i-)WGS) and methane conversion on two representative perovskite-type materials, $La_{0.6}Sr_{0.4}FeO_{3-\delta}$ (LSF) and $SrTi_{0.7}Fe_{0.3}O_{3-\delta}$ (STF), respectively. The latter two are deemed relevant materials due to their different iron content. As iron is mostly suspected to be the center of catalytic reactivity due to its pronounced redox behavior, we aim at providing data to what extent this is true. In fact, combined structural characterization (mostly by TEM) and catalytic testing will indicate that this is only part of the truth, and a more complex behavior, especially with respect to the quality of oxygen vacancies, must be assumed. In due course, the stability of the perovskite (surface) structure during a full catalytic cycle including preoxidation and reduction will be monitored. Therefore, catalytic measurements in a recirculating batch reactor setup especially designed for the measurement of small reaction rates,[72] structure-determining methods (analytical high-resolution electron microscopy and X-ray diffraction), and Raman spectroscopic measurements were jointly applied.

## 2. EXPERIMENTAL METHODS

**2.1. Preparation of the Perovskite Powders.** $La_{0.6}Sr_{0.4}FeO_{3-\delta}$ was prepared via the Pecchini route:[73] respective amounts of $La_2O_3$, $SrCO_3$, and metallic Fe (all three at least 99.95% pure, Sigma-Aldrich) were dissolved in $HNO_3$ (double distilled, Sigma-Aldrich). All three solutions were mixed, and citric acid (99.9995% pure, Sigma-Aldrich) was added to the solution in a 20% excess with respect to the cations. The solution was heated, and after the evaporation of water the mixture formed a highly viscous foam, which finally decomposed in a spontaneous combustion. The obtained powder was calcined for 2 h at 1000 °C in air; the product was ground in a mortar and checked for phase purity by X-ray diffraction (XRD).

The $SrTi_{0.7}Fe_{0.3}O_{3-\delta}$ powder was obtained by a solid state reaction from $SrCO_3$, $TiO_2$, and $Fe_2O_3$ (all three at least 99.98% pure, Sigma-Aldrich). The educts were thoroughly mixed, calcined at 1000 °C for 2 h, ground in a mortar, and calcined a second time at 1250 °C for 2 h. The product was again ground and also checked for phase purity by XRD. Surface areas using the BET method were determined for both samples to be around 0.4 $m^2\ g^{-1}$. BET surface areas were measured with a Quantachrome Nova 2000 surface and pore size analyzer.

For catalytic measurements the powders were used as obtained by the procedures described above. For pulsed laser deposition (PLD) of thin films, targets of LSF were prepared by isostatically pressing the powders and sintering the green bodies at 1250 °C for 5 h in air.

**2.2. Electrode Preparation and Electrochemical Impedance Spectroscopy.** Thin films of LSF were deposited on yttria-stabilized zirconia (100) single crystals (YSZ, 9.5 mol % $Y_2O_3$, CrysTec, Germany) by PLD. For electrochemical measurements in reducing conditions a current collecting thin film grid was deposited prior to the PLD process by sputtering 10 nm Ti on YSZ followed by 100 nm of Pt. This thin film was micropatterned by a photolithography process and Ar-ion beam etching. For the subsequent PLD process a KrF excimer laser (Lambda COMPexPro 201F) with 248 nm wavelength was used to ablate the LSF target. The deposition was done in $4 \times 10^{-2}$ mbar of pure oxygen with a laser pulse repetition rate of 5 Hz, a nominal laser pulse energy of 400 mJ, and a YSZ substrate temperature of 650 °C (controlled by a pyrometer; Heitronics, Germany). Typical film thicknesses were 200 ± 20 nm. From these films with buried current collectors circular microelectrodes were produced by again carrying out a photolithography process and an Ar-ion beam etching step. A


DOI: 10.1021/acs.jpcc.5b02947
J. Phys. Chem. C 2015, 119, 11739−11753

scanning electron microscopy (SEM) image of a circular LSF electrode with buried Ti/Pt current collector is shown in Figure S1, and a schematic depiction of the thin film electrode setup is shown in Figure S2. In a previous impedance study on STF electrodes with buried Pt current collectors,[43] it was shown that the surface exchange resistance and the chemical capacitance of the electrode can be extracted from the low-frequency part of the impedance spectra.

Impedance spectroscopy measurements on these thin film electrodes were carried out in a home-built microcontact setup. It allows contacting of individual electrodes by Pt/Ir tips, which can be accurately positioned by piezoelectric high-precision actuators (Newport Agilis). The atmosphere in the setup was either synthetic air or ~2.5% $H_2$/~2.5% $H_2O$/balance Ar, and the electrode temperature was about 610−620 °C. Further details regarding the microcontact setup are given in ref 74. Impedance measurements were conducted with an Alpha-A high performance frequency analyzer with POT/GAL 30 V 2A test interface (both Novocontrol, Germany) in a frequency range between 10 mHz and 1 MHz at an ac voltage of 10 mV (root-mean-square, rms). Impedance data analysis was done by the complex nonlinear least-squares fitting software Z-View 3.1 (Scribner, USA).

**2.3. Catalytic Measurements.** The catalytic measurements on LSF and STF powder samples were exclusively performed in a recirculating batch reactor (ca. 13 mL volume) especially designed for detection of very small reaction rates. Details of the construction are discussed elsewhere.[72] Detection of the reactants and products was carried out by a quadrupole mass spectrometer (QMS) attached to the reaction chamber via a capillary leak. For a typical inverse water-gas shift experiment, a 1:4 mixture of $CO_2$ and $H_2$, delivering the right stoichiometry for a potential methanation reaction, as well as 25 mbar of $H_2O$ to ensure thermodynamically stable conditions, was filled into the reaction chamber of the batch reactor. For the water-gas shift reaction, a 1:1 ratio of CO and $H_2O$ (25 mbar each) was used. Subsequently, the mixture was heated with 5 °C $min^{-1}$ from room temperature to 600 °C, followed by isothermal periods of variable duration before the final cooldown. Ar (~7.5 mbar) was additionally admitted to all reaction mixtures to correct all other signals for the continuous gas withdrawal through the leak. The mass-to-charge ratios $m/z$ = 2 ($H_2$), 15 and 16 ($CH_4$), 18 ($H_2O$), 28 (CO), 40 (Ar), and 44 ($CO_2$) were routinely monitored. The CO signal was corrected for the contribution from $CO_2$ fragmentation in the mass spectrometer. The QMS intensities were calibrated (i.e., converted into partial pressure given in mbar) using external calibration standards. Further experimental details are given in the respective figure captions.

A brief account of the mass and heat transport limitations should be given at this point. We exclude effects of mass transport and pore diffusion limitation, since the samples are used in quite small amounts (100−200 mg) of loose powder, which can be quickly penetrated by the reaction gas. Note that the same catalyst setup that has been used for the studies on comparable systems, where much higher reaction rates were accurately measured. Heat transfer limitation is also judged to play a minor role since local temperature effects are excluded due to the low reaction rates, and generally, heat transfer via the gas phase is enhanced due to the deliberate admission of He to the reaction mixture (1 bar total pressure).

**2.4. Volumetric Adsorption.** The volumetric adsorption measurements were conducted in an all-quartz apparatus described in detail elsewhere (reactor volume: 32 mL),[75] additionally using a Balzers QMA125 quadrupole mass analyzer and a Linn furnace operating up to 1220 °C. All perovskite powder samples were subjected to a pretreatment in flowing oxygen up to 600 °C, with an isothermal period at 600 °C for 1 h before finally cooling down. After this oxidation step, the system was evacuated at room temperature to a base pressure of about $5 \times 10^{-7}$ mbar after the aforementioned oxidation treatment, and a defined amount of ~100 mbar of $H_2$ was admitted. Subsequently, the samples were heated to 600 °C at a rate of 10 °C $min^{-1}$, followed by an isothermal period at 600 °C for 1 h before cooling to room temperature. For better comparison also to literature-reported data, all mass spectrometer data (in mbar) were converted into micromoles on the basis of the ideal gas equation, with subsequent normalization to sample mass and surface area. Cleaning of the gases was performed using either a liquid $N_2$ (for $H_2$) or a liquid $N_2$/ethanol cooling trap (for $O_2$). Note that the term "adsorption" (better viewed as "uptake") in this case also includes actual hydrogen "consumption" reactions, such as bulk reduction or hydrogen insertion into the perovskite lattice. As a zeolite trap is used to quantitatively remove reaction-formed water from the volumetric chamber, accurate absolute quantification of the second mechanism is presently not possible. However, as will be shown later, different behavior of both STF and LSF in their oxidized and reduced states, respectively, is an experimental matter of fact. Although the exact bulk oxygen and hydrogen stoichiometry of the samples in different states of reduction is not known due to the above-mentioned obstacle, we nevertheless decided to use a specific partially reduced "prereaction" state prior to catalytic testing (see section 2.3). Prereduction at 873 K in dry hydrogen was on the one hand done gently enough to avoid reductive decomposition of the samples. On the other hand, substantial formation of additional oxygen vacancies (beyond those already induced by the prereduction) during e.g. a subsequent temperature-programmed water-gas shift reaction experiment could be largely suppressed by the reductive pretreatment and by performing the catalytic experiment at $T \leq T_{\text{prereduction}}$. Thus, true catalytic experiments with complete reactant/product mass balance became feasible.

**2.5. Transmission Electron Microscopy.** Structural characterization of the samples was carried out by two types of electron microscopes. Bright-field (high-resolution) imaging and high-angle annular dark-field imaging were carried out using a 200 kV FEI TECNAI F20 STWIN analytical (scanning) transmission electron microscope ((S)TEM) equipped with a Tridiem energy filter. High-resolution, high-angle annular dark-field imaging EEL and EDX spectroscopy were performed using an aberration-corrected FEI Titan microscope operating at 300 kV. Electron-energy loss spectra are background-corrected and corrected for plural scattering. Prior to imaging, the samples were sputter-cleaned to remove surface carbon impurities. For the high-resolution images, the STF and LSF samples were suspended in acetone and cleaned in an ultrasonic bath prior to mounting on a holey carbon film. In the case of HAADF images to be taken, the samples were heated to 80−100 °C under high-vacuum conditions ($4 \times 10^{-4}$−$10^{-6}$ mbar) prior to imaging.

**2.6. X-ray Diffraction.** X-ray powder diffraction data were collected at ambient conditions with a Bruker AXS D8-Advance powder diffractometer using Cu K$\alpha_1$ and Cu K$\alpha_2$ radiation ($\lambda_1$ = 1.5406 Å; $\lambda_2$ = 1.5444 Å; 40 kV; 40 mA). The diffractometer



DOI: 10.1021/acs.jpcc.5b02947
J. Phys. Chem. C 2015, 119, 11739−11753

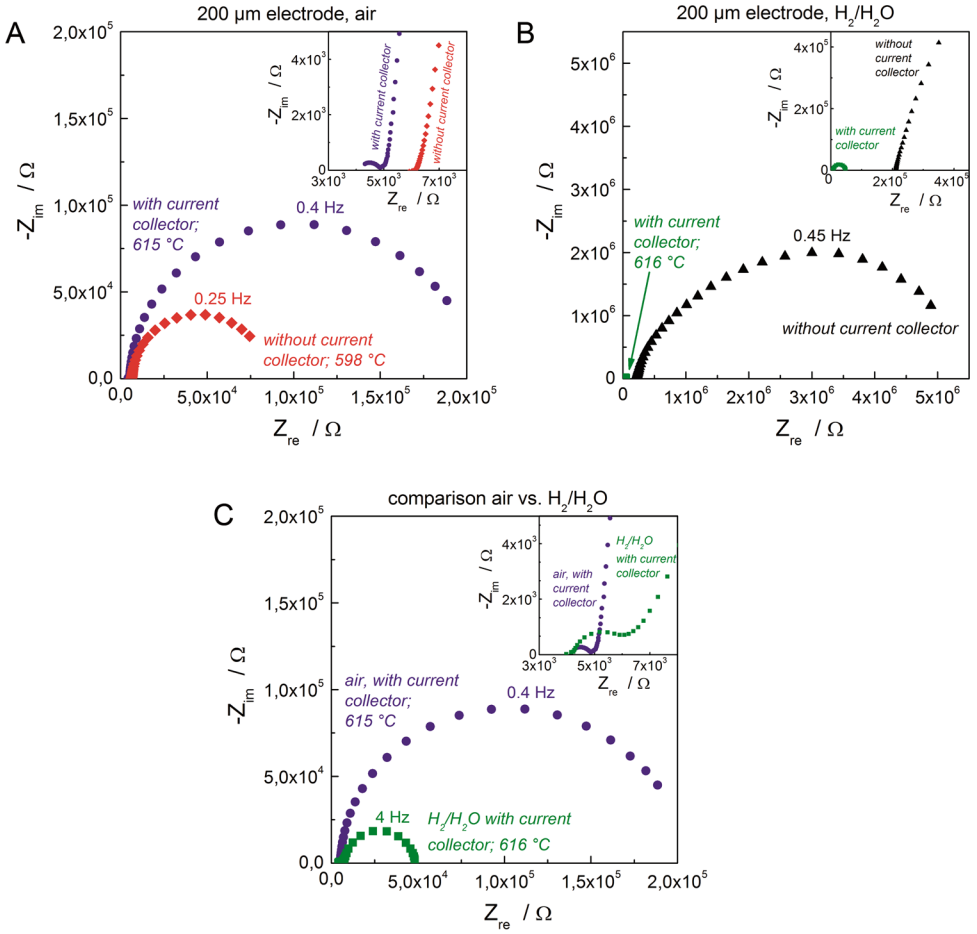


**Figure 1.** Impedance spectra (Nyquist plots) measured on 200 $\mu$m thick LSF microelectrodes with and without buried Ti/Pt current collectors. The insets in the top right corners show magnifications of the high-frequency region of the spectra. The measurements were performed in air (A) as well as in reducing atmosphere, ~2.5% $H_2$/~2.5% $H_2O$/balance Ar (B). The spectra measured on LSF with current collectors in air (from A) and in reducing atmosphere (from B) are compared in (C).

exhibits a Bragg−Brentano reflection geometry with $\theta$−$\theta$ coupling and parallel beam optics. An energy-dispersive Si(Li) semiconducting Sol-X detector was used. Data acquisition was performed in the $2\theta$ range between 2° and 90° with a step width of 0.02° and a counting time of 3 s under sample rotating conditions. The sample itself was prepared on a Si single crystal holder with suppressed background intensity.

**2.7. Raman Spectroscopy.** Confocal Raman spectra of the polycrystalline samples in the range of 50−3800 $cm^{-1}$ were recorded with a Horiba Jobin Yvon Labram-HR 800 Raman microspectrometer. The samples were excited using the 532 nm (2.33 eV) emission line of a frequency-doubled 25 mW Nd:YAG laser under an Olympus 100× objective lens with a numerical aperture of 0.9 and additionally He−Ne laser (633 nm) for detection of luminescence effects. The size of the laser spot on the surface was approximately 1 $\mu$m in diameter. The scattered light was dispersed by an optical grating with 1800 lines $mm^{-1}$ and collected by a (Peltier-cooled) 1024 × 256 open-electrode CCD detector confocally coupled to the focal point of the sample. The spectral resolution, determined by measuring the fwhm of the Rayleigh line, was below 2 $cm^{-1}$ (using a slit width of 100 $\mu$m). The spectra were recorded unpolarized at ambient conditions. The accuracy of the Raman line shifts, calibrated by measuring a silicon standard (522 $cm^{-1}$), was in the order of 0.5 $cm^{-1}$. Spectra were recorded from a representative grain of the samples as a single measurement (10 s integration time). No averaging of spectra has been performed. Note that the spectra are not background corrected or fitted.

## 3. RESULTS AND DISCUSSION

**3.1. Electrode Kinetics of LSF in Oxidizing and Reducing Atmosphere.** Impedance spectra obtained on LSF electrodes with and without buried Ti/Pt current collectors are depicted in Figure 1. Both types of electrodes were characterized in air (see Figure 1A) as well as in reducing ~2.5% $H_2$/~2.5% $H_2O$/Ar atmosphere (cf. Figure 1B). In air the impedance spectra consist of three relatively well separated features. In the high-frequency range (see inset in Figure 1A) a real axis intercept can be observed, which can be attributed to the spreading resistance of ion conduction in YSZ.[76] This resistance, together with the size of the circular microelectrodes, was used to obtain the true temperature of the measured microelectrodes (for details regarding this calculation please refer to refs 77 and 78). The arcs in the medium- and low-frequency region can be related to an ionic transfer resistance at the electrode/electrolyte interface and to the oxygen incorporation resistance at the electrode surface, respectively.[76] In the case of the electrode with buried current collector the interfacial resistance and the dominating surface resistance are increased, which can be easily explained by the ion blocking character of the current collectors. Thus, only a


DOI: 10.1021/acs.jpcc.5b02947
J. Phys. Chem. C 2015, 119, 11739−11753

smaller part of the electrode/electrolyte interface as well as of the electrode surface is available. Taking the geometry of the grid into account (3/4 of the interface covered with metal, 1/4 free interface), the electrode kinetics of both types of electrodes (with and without grid) in air can be regarded as very similar.

In reducing atmosphere the situation strongly changes (cf. Figure 1B). Here, the spectrum measured on LSF without current collector is both qualitatively and quantitatively significantly different than the spectra obtained in oxidizing atmosphere. First, the high-frequency axis intercept is about 2 orders of magnitude larger than one might expect from the nominal size of the electrode. Second, in the medium-frequency regime an additional shoulder appears, and third, the total polarization resistance of the electrode is more than 1 order of magnitude larger than in air (cf. Figure 1A). From this result one might conclude that LSF is a rather poor electrode for hydrogen oxidation. However, the finding that the high-frequency intercept—which is expected to be the spreading resistance of ion conduction in YSZ—is much too large for the nominal electrode size is a strong indication that owing to a high sheet resistance in the LSF film only a rather small part of the electrode around the tip contact is electrochemically active.[41]

This interpretation is further supported by the fact that in the case of LSF electrodes with buried current collector the high-frequency real axis intercepts are close to those of spectra measured in air (see inset in Figure 1C). Moreover, the total electrode impedance of LSF with current collector measured in $H_2/H_2O$ is within the same order of magnitude as the electrode resistance in air (see Figure 1C). Considering the active areas of the two electrodes ($0.79 \times 10^{-4}$ $cm^2$ for LSF in air and $3.14 \times 10^{-4}$ $cm^2$ for LSF in $H_2/H_2O$), one can even calculate almost identical area-specific polarization resistances of 16 and 15 $\Omega \cdot cm^2$ for LSF under oxidizing and reducing conditions, respectively.[a] Since the inverse polarization resistances are a direct measure for the exchange current and thus the exchange rates at the electrode surfaces, at ca. 620 °C the catalytic activitiy of the LSF surface for oxygen reduction and hydrogen oxidation is rather similar.

In a previous impedance study on STF model electrodes in reducing atmosphere a surface resistance of ca. 200 $\Omega \cdot cm^2$ was obtained.[43] This comparison reveals that LSF is significantly more active for $H_2$ oxidation than STF. Corresponding differences in the "conventional" catalytic behavior of the two materials will be discussed below on the basis of their specific oxygen vacancy/lattice oxygen reactivities. In particular, vacancies in LSF are shown below (section 3.2) to be much more reactive with respect to quenching by water splitting (the reverse process of hydrogen oxidation by lattice oxygen), and the associated water affinity of the vacancies is clearly higher than on STF.

Taking into account the above-mentioned area-related polarization resistance, an application of LSF in porous SOFC anodes may lead to electrodes with polarization resistances comparable to nowadays used porous paste cathodes. This potential applicability, however, raises the question of compatibility of LSF anodes with carbon based fuels such as methane. Thus, besides the fundamentally interesting questions regarding surface activity of perovskite-type catalysts (as discussed in the Introduction), the catalytic activity of LSF for reactions such as water-gas shift and methane activation needs to be investigated in detail as shown in the following sections.

### 3.2. Catalytic Experiments and Volumetric Adsorption.

Before focusing on the structural changes occurring on the STF and LSF perovskite-type systems upon oxidative and reductive pretreatments or during a catalytic cycle, the activities for the water-gas shift and methane conversion reaction are outlined. This also includes a discussion of temperature-programmed hydrogen uptake experiments, which very much adds to the understanding of the associated temperature-programmed catalytic reaction profiles. The term "adsorption" in this respect includes all hydrogen uptake or consumption processes lowering the hydrogen concentration in the gas, including adsorption, absorption in the oxide, but also water formation by oxide reduction.

Figure 2 shows two sets of temperature-programmed inverse water-gas shift reaction runs on STF with different sample

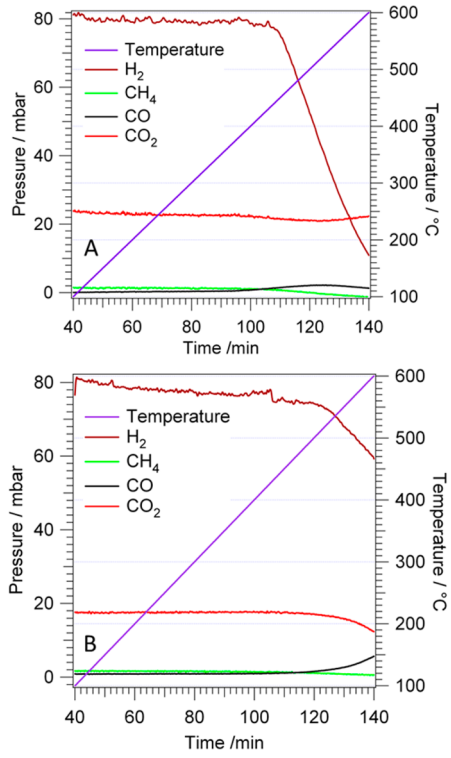


**Figure 2.** Temperature-programmed reaction profiles of the inverse water-gas shift reaction on STF without (panel A) and with (panel B) prereduction in hydrogen at 600 °C (1 h, 1 bar). Heating rate: 5 °C $min^{-1}$, 1:4 starting mixture of $CO_2$ and $H_2$ including 25 mbar of $H_2O$, 7.5 mbar of Ar, and He added to 1 bar total pressure.

pretreatments. A preoxidation at 400 °C in oxygen for 1 h was applied in both experiments to ensure identical starting conditions. The experiment shown in panel A was done directly after this oxidation step; i.e., it refers to the fully oxidized STF catalyst. In the case of the catalyst shown in panel B, a reductive treatment at 600 °C (1 h, 1 bar hydrogen) was performed for the above-mentioned reasons (see section 2.4.) after the preoxidation step and before the catalytic experiment. Both panels are shown as partial pressure vs time and temperature plots. The mass spectrometer signals of $H_2$, $CH_4$, CO, and $CO_2$ were recorded. As can be clearly seen in both panels, the reduction/reaction starts in the case of the fully oxidized sample at ~430 °C, and on the prereduced one at around 500 °C, as indicated by the pronounced decrease of the $H_2$ signal. As the inverse water-gas shift reaction



DOI: 10.1021/acs.jpcc.5b02947
J. Phys. Chem. C 2015, 119, 11739−11753

$$H_2 + CO_2 \Leftrightarrow CO + H_2O$$

also consumes $CO_2$ and produces CO in a fixed stoichiometric amount, the profile shown in panel B is that of a "true" inverse water-gas shift reaction (i-WGSR) with stoichiometric reactant consumption and product formation (the water signal is not displayed since a zeolite trap was used in the TPR experiments; see section 2.4). In contrast, stoichiometric CO formation is apparently not the case for the fully oxidized sample, given the substantially higher hydrogen consumption shown in panel A, largely exceeding the stoichiometric amount with respect to CO. Neither is $CO_2$ simultaneously consumed nor sufficient CO produced alongside hydrogen being reacted off. This behavior can only be consistently interpreted in terms of a reduction of the perovskite catalyst by hydrogen forming oxygen vacancies in the perovskite lattice,[11,60,61,63,80−83] which remain mostly unreactive toward $CO_2$, and releasing $H_2O$ into the reaction mixture; in Kröger−Vink notation this reaction reads

$$H_2 + O_O^{\times} + 2h^{\bullet} \rightarrow H_2O + V_O^{\bullet\bullet}$$

From a catalytical point of view, the water-gas shift equilibrium is obviously disfavorably shifted toward $CO_2$ due to the ongoing hydrogen depletion of the reaction gas mixture at these elevated temperatures. This behavior can be regarded as a strong indication that a suitable prereduction of the perovskite-type catalyst is essential for generating sufficiently reactive vacancies capable of stoichiometric $CO_2$ reduction and thus stoichiometric turnover of the reactants toward the water-gas shift equilibrium.

A similar catalytic inverse water-gas shift reaction profile was observed for the corresponding LSF powder sample after a reductive pretreatment: under comparable experimental conditions, the reaction of $H_2$ and $CO_2$ to CO (and $H_2O$) starts at around 500 °C. As observed for STF, also the prereduced LSF shows a stoichiometric inverse water-gas shift reaction profile (cf. Figure 6 A); further details of the LSF catalyst will be discussed below.

To further shed light on the hydrogen reducibility of LSF and STF, temperature-programmed hydrogen consumption measurements after oxidation at 600 °C were performed (see Figure 3). According to these measurements, on LSF hydrogen starts to be steadily consumed at around 200 °C with a notable rate increase around 350 °C. At least two discernible steps in the hydrogen consumption are visible. A very similar TPR pattern was observed on STF, although the onset temperature is shifted by about 60−260 °C. The $H_2$ consumption appears to proceed at a slower rate compared to LSF, and no clearly discernible steps were observed. Saturation of hydrogen uptake is apparently not even reached at the highest studied temperatures for both perovskite samples, as can be deduced from the quite pronounced isothermal uptake, accounting for yet another 200−300 $\mu$mol $m^{-2}$ hydrogen consumption at 600 °C within 60 min. Therefore, we might infer considerable kinetic limitations prevailing even at 600 °C. Upon recooling, no additional hydrogen consumption was observed. Most notable, however, is the outstanding amount of consumed hydrogen in the course of the experiment. After the isothermal period, a total amount of 3500 $\mu$mol $m^{-2}$ consumed hydrogen on LSF and about 2000 $\mu$mol $m^{-2}$ on STF has been determined, which is approximately 300 times the amount measured on highly reducible "simple" oxides, such as $In_2O_3$, under comparable experimental conditions.[84]

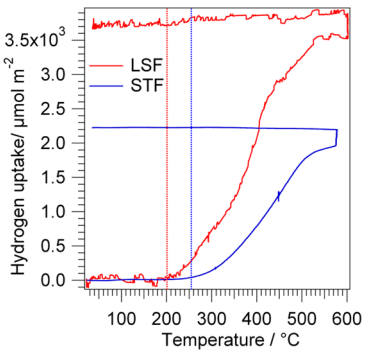


**Figure 3.** Volumetric hydrogen uptake measured on STF and LSF. Heating rate from room temperature to 600 °C at 10 °C $min^{-1}$ followed by an isothermal perion at 600 °C for 1 h. Initial hydrogen pressure: 100 mbar. The measurement was performed using a zeolite trap in the cold part of the reaction chamber for effective removal of water resulting from the oxide reduction.

As already mentioned above, in the case of both perovskite-type catalyst powders the reductive treatment leads to an oxygen nonstoichiometry, i.e., to a formation of oxygen vacancies and the corresponding modification of the electronic charge carrier concentrations. From the above-mentioned amounts of consumed hydrogen the degree of reduction $\delta$ of the two perovskite-type catalysts (i.e., their oxygen nonstoichiometry in the prereduced state) can be estimated. For $La_{0.6}Sr_{0.4}FeO_{3-\delta}$ and $SrTi_{0.7}Fe_{0.3}O_{3-\delta}$ values of ca. 0.2 and ca. 0.1 were obtained, respectively (only in rough approximation, i.e., upon excluding the formation of bulk hydrogen species obscuring this mass balance; compare section 2.4). It is already worth to mention that effects of pronounced reduction of perovskites via reaction of lattice oxygen with $H_2$ are also visible in the respective Raman spectra and X-ray diffractograms (cf. Figures 9 and 10 and related discussion below). This indicates that the perovskite structural entity as a whole is stable, but nevertheless structurally slightly altered by the hydrogen treatment, at least at temperatures $T \geq 600$ °C.

In previous studies on simpler oxides, like $In_2O_3$[84] or $Ga_2O_3$,[85] the reactivity in the (inverse) water-gas shift equilibrium was determined to be strongly dependent on the prereduction degree of surface and bulk regions. Thus, associated tests on the oxygen vacancy quenching ability were performed on LSF and STF powders by exposing the prereduced catalysts to 25 mbar of $H_2O$ vapor and performing a TPR experiment (Figure 4). Interestingly, no reaction of $H_2O$ on a hydrogen prereduced sample has been observed for STF (inset: the small water uptake at low temperatures is an experimental artifact), in contrast to LSF (main panel), where a clear hydrogen signal, likely arising from the quenching of the introduced vacancies via dissociative decomposition of $H_2O$, is observed. The potential implications of this result on the promotion of electrochemical water splitting are already mentioned in section 3.1; those regarding the activity toward attaining the (inverse) water-gas shift equilibrium are jointly discussed in the context of Figure 6 (see below). Note that under the chosen experimental reduction conditions (static reduction), no signs of segregation of metallic iron are visible, although we cannot exclude the formation of undetectable modest amounts of metallic iron. TEM experiments show no pronounced iron oxide segregation after room temperature


DOI: 10.1021/acs.jpcc.5b02947
J. Phys. Chem. C 2015, 119, 11739−11753

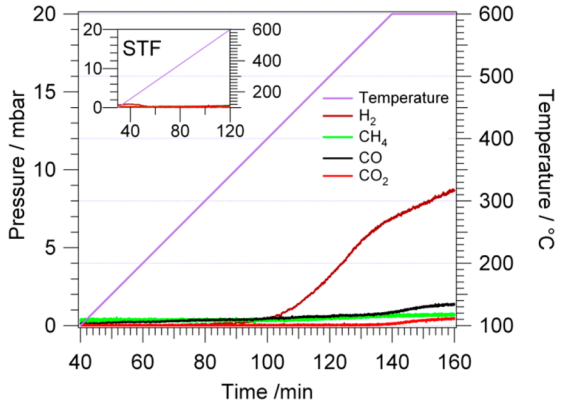


**Figure 4.** Reactivity of water with oxygen vacancies introduced by hydrogen reduction as shown in Figure 3. LSF is shown in the main panel and STF as the inset. Both samples were prereduced in hydrogen at 600 °C (1 bar, 1 h), recooled to room temperature, and exposed to about 25 mbar of $H_2O$ vapor, before a temperature-programmed reaction (TPR) was started. The heating rate was set to 10 °C $min^{-1}$.

exposure of a reduced sample to ambient (redissolution of ionic iron in the perovskite lattice is therefore excluded).

In Figure 5 the activity of LSF and STF in the inverse water-gas shift reaction is depicted (after prereduction at 600 °C). In

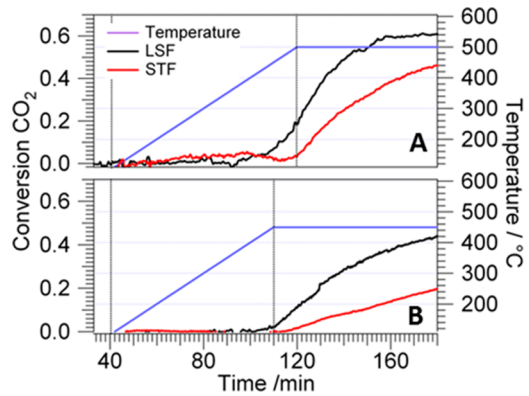


**Figure 5.** Surface-area-normalized temperature-programmed reaction profiles of the inverse water-gas shift reaction shown as $CO_2$ conversion vs time plots at two different temperatures (450 °C: panel B; 500 °C: panel A) with extended isothermal periods for both fully oxidized STF and LSF to reveal the inherently different catalytic activity. Heating rate: 5 °C $min^{-1}$, 1:4 starting mixture of $CO_2$ and $H_2$ with 25 mbar of $H_2O$, 7.5 mbar of Ar, and He added to 1 bar total pressure.

both panels A and B, the time-dependent conversion of $CO_2$, normalized to the sample surface, as well as the reaction temperature is plotted versus the reaction time. The latter is composed of a heating period (5 °C $min^{-1}$) followed by a prolonged isothermal period in order to quantify the respective isothermal reaction rate at a given conversion from the respective slope of the conversion curve. Panel A shows isothermal experiments at 500 °C and panel B those at 450 °C. For both temperatures and at low conversion values, the normalized $CO_2$ conversion rate on LSF is always higher compared to that on STF. At conversions approaching the water-gas shift equilibrium, a readout of the slope makes no more sense anyway. As during the isothermal periods increasing conversion is observed, this allows the determination of surface area-normalized and thus comparable reaction rates (at the same $CO_2$ conversion), given in mbar $min^{-1}$ $m^{-2}$. The extracted reaction rates from the isothermal range of the conversion vs time plots are summarized in Table 1. Note that

**Table 1. $CO_2$ Conversion Rate Measured on LSF and STF at Two Different Temperatures[a]**

| | $CO_2$ conversion rate (mbar $min^{-1}$ $m^{-2}$) | |
|---|---|---|
| temperature (°C) | LSF | STF |
| 450 | 3.6 | 1.7 |
| 500 | 10.1 | 6.9 |

[a]The rates were determined in both cases between 20 and 30% conversion.

the $CO_2$ conversion was calculated as the ratio of the $CO_2$ pressure and total pressure of $CO_2$ and CO, which is equivalent to the $CO_2$ pressure in the beginning. The temperature-dependent water-gas shift equilibrium for the chosen experimental conditions is shown in Figure S3 of the Supporting Information and very much coincides with the experimental values.

At 500 °C, $CO_2$ conversions of about 40% and 60% are obtained on STF and LSF, respectively, whereby the isothermal reaction time of ∼1 h at 500 °C is sufficient to approach the (i-)WGSR equilibrium only on LSF. A qualitative comparison with the water-gas shift reaction on other perovskite-type oxides, namely $La_{1-x}Ce_xFeO_3$ and $La_{0.9}Sr_{0.1}Cr_{1+x}Mn_xCo_x$-$O_{3\pm\delta}$,[27,29] reveals that especially on the latter (again measured at 450 and 500 °C) much shorter contact times (of a few minutes) with the catalyst are sufficient to achieve equilibrium conversion, especially if the chromium content is high. We therefore conclude that our specific activities may rather compare to the respective Mn/Co-rich samples.

Note also that in combination with the hydrogen TPR experiments shown in Figure 3 the reaction profiles in Figures 2 and 4 generally suggest a potential influence of the vacancies (formed by reduction) on the catalytic properties in the water-gas shift equilibrium. In general, WGSR activity of different perovskite materials is well-known[50−53] and almost always directly linked to the number of oxygen vancancies, as derived from chemical looping pulse experiments with sequential pulsing of reactants. Note in this respect, however, that the WGSR reaction mixture is therefore not admitted simultaneously, and generally, no difference is made regarding the qualitative nature of the oxygen vacancies.

Vacancy formation is in due course usually connected with the amount of the iron content of the material. However, correlating the reactivities to the amount of the initial number of vacancies introduced by the hydrogen treatment (and therefore to the amount of iron) is not feasible: in doing so, one has to assume that (i) all the hydrogen consumption leads to water formation (hence, the amount of vacancies represents only the upper limit) and (ii) the amount of vacancies does not change during the reaction. As discussed above, (i) is clearly not fulfilled. In view of Figure 4, it is also obvious that (ii) does not hold, since the reactivity toward water is different on STF and LSF. As for the direct correlation to the bulk iron content, note also that the surfaces of both perovskites after the catalytic runs are predominantly SrO-terminated (cf. section 3.3 and ref 70).

In particular, our results illustrate the qualitative differences of surface (near) defect/vacancy reactivity on these materials


DOI: 10.1021/acs.jpcc.5b02947
J. Phys. Chem. C 2015, 119, 11739−11753

and the necessity to link the "apparent" activation barriers (see below) to the specific oxygen affinity of such (to some extent likely Fe- or Ti-containing) redox-active centers. Moreover, it appears mandatory to link the surface area normalized "macroscopic" catalytic activity to their effective (i.e., not bulk-proportional) surface concentration, which is determined by the specific segregation chemistry of the surfaces under realistic reaction conditions.

Eventually, an Arrhenius estimation of the apparent activation energy for the i-WGSR based on the initial rates at low conversions yielded ca. 90 and ca. 130 kJ $mol^{-1}$ for LSF and STF, respectively.

Figure 6 summarizes a set of reactivity data necessary for a thorough understanding of the (inverse) water-gas shift and

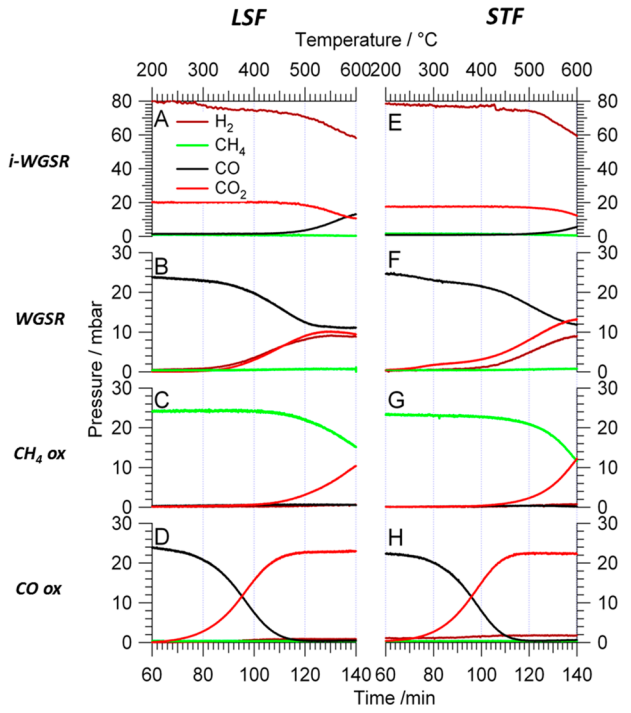


**Figure 6.** Temperature-programmed reaction profiles on LSF (panels A–D) and STF (panels E–H). Panels A and E: i-WGSR, $CO_2 + H_2 \rightarrow CO + H_2O$, 20 mbar of $CO_2$ and 80 mbar of $H_2$ including 25 mbar of $H_2O$ (preoxidation at 400 °C, prereduction at 600 °C). Panel E, for the sake of clarity, again shows the reactivity profile of Figure 2A; panels B and F: WGSR, $CO + H_2O \rightarrow CO_2 + H_2$ 25 mbar CO and 25 mbar $H_2O$ (preoxidation at 400 °C, prereduction at 600 °C). Panels C and G: methane oxidation on initially fully oxidized samples, $CH_4 \rightarrow CO_2 + H_2O$, 20 mbar of $CH_4$ (preoxidation 400 °C). Panels D and H: CO oxidation on initially fully oxidized STF and LSF, $CO \rightarrow CO_2 + V$, 25 mbar of CO (preoxidation at 400 °C).

methane reactivity. For direct comparison, panels A and E again show the inverse water-gas shift reactivity profiles on LSF and STF after prereduction (note that Figure 6E corresponds to Figure 2A). For comparison to the inverse water-gas shift experiments, panels B and F show the experiments in the water-gas shift direction. Experiments have been conducted both on fully oxidized ($O_2$, 400 °C, panels D and H) and prereduced ($H_2$, 600 °C, panels B and F) samples. As for the water-gas shift activity, CO is reacted off with simultaneous $CO_2$ and $H_2$ production on both perovskites, if the perovskite powder is prereduced (cf. Figure 6, panels B and F). The onset temperature of reaction is at about 300 °C, therefore between the one typically observed for conventional low-temperature copper-based WGS catalysts like $Cu/ZnO/Al_2O_3$[86] and iron-based catalysts used for higher temperatures.[87,88] On fully oxidized samples only $CO_2$ formation without $H_2$ production was observed (cf. Figure S2). Apparently, in the latter case, total oxidation of CO to $CO_2$ is the only observed reaction channel, occurring via reduction of reactive lattice oxygen by CO, but not primarily via a catalytic water-gas shift reaction cycle. This is directly proven by the simple reduction of the fully oxidized perovskite systems by CO without water (Figure 6, panels D and H), which both show direct transformation of CO into $CO_2$. Note in this respect that the start temperature of the water-gas shift reaction on both catalysts is lower as compared to the inverse direction (compare panels A and B as well as E and F in Figure 6). This implies that an "additional" low-temperature prereduction by CO (thus forming $CO_2$) takes place (see also the "two-step" WGSR reaction profile on STF, Figure 6F). Obviously, the catalyst adapts itself to the equilibrium state in a kinetically different manner depending on the starting conditions ($CO_2$ and $H_2$ for the inverse; CO and $H_2O$ for the water-gas shift reaction).

As it is well-known from experiments on simpler oxide systems (e.g., $Ga_2O_3$[85] or $In_2O_3$[84]), the (inverse) water-gas shift reaction can in principle follow different distinct reaction pathways, depending on the temperature-dependent relative contribution of surface adsorbate and defect chemistry (i.e., oxygen affinity of vacancies/reduced surface centers vs stability of adsorbed intermediates): a vacancy-mediated mechanism (VMM), a formiate-mediated mechanism (FMM), or following a pathway including CO dissociation. On $Ga_2O_3$, FMM and VMM pathways were observed, depending on the degree of reduction (i.e., the number of vacancies), degree of surface hydroxylation, and temperature. On $In_2O_3$, due to its outstanding reducibility, the VM mechanism was strongly dominating already at low temperatures. In due course, the question arises, which pathway is predominantly followed on the more complex perovskite systems? Our results suggest that on LSF the VM mechanism is predominantly observed but appears to play a minor role on STF, as can be deduced from the water-quenching experiments shown in Figure 4. At the present stage of experiments, we cannot exclude a possible contribution of an FM mechanism on LSF, even more on STF, where future directed *in situ* FTIR experiments will definitely show if, and in which temperature regime, the reaction profile observed in panel F follows the latter mechanism. As can be deduced from the inability of the vacancies to dissociate water (Figure 4), the VM mechanism is at least not predominantly prevailing on STF. Most important in this respect is a comparison of the "depth" of oxide reduction and further reducibility in $H_2$ at 600 °C, i.e., a prereduced state compared with the fully oxidized state in Figure 2: upon deep reduction higher temperatures are required to (re)establish reactive reduced centers in course of the catalytic inverse water-gas shift reaction cycle (Figure 6A,E). In line with our results, recent studies by Diebold et al. on the WGSR mechanism on $Fe_3O_4$ revealed that indeed the FMM is dominant at low temperatures via OH groups and formates from OH and CO. At higher temperatures ($T > 520$ K), a defect-mediated water-splitting mechanism (Mars–van Krevelen type) is shown by STM.[89] CO dissociation, on the contrary, is certainly correlated with the presence of metallic iron. If the hydrogen partial pressure and the temperature are high enough, the presence of iron


DOI: 10.1021/acs.jpcc.5b02947
J. Phys. Chem. C 2015, 119, 11739–11753

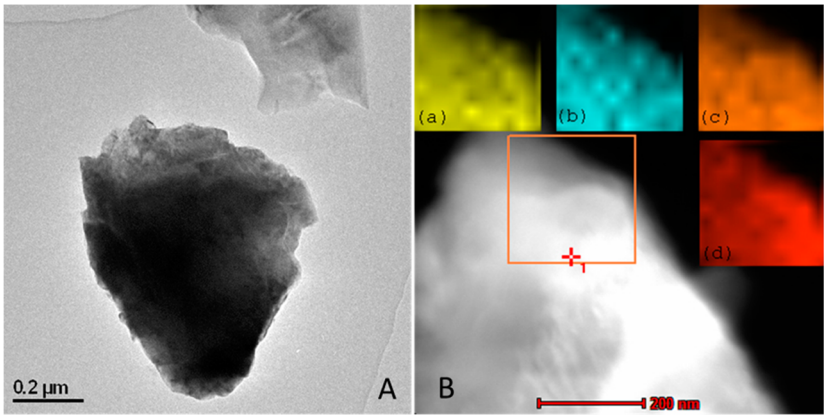


**Figure 7.** Bright-field overview TEM image of a representative STF grain (panel A) and STEM-HAADF image of an extended region on the edge of a STF grain to emphasize the chemical homogeneity of the sample (panel B). EDX maps of the Ti−K (a), Fe−K (b), Sr−L (c), and O−K (d) edges are shown as false color insets and were collected in the squared region as indicated.

carbide/metallic iron cannot be excluded, but if then the mechanism is still the same, remains an open question.

Note that after prereduction at 600 °C the hydrogen is pumped off and the sample recooled in vacuum—this treatment most probably removes the major part of the adsorbed hydrogen. Admission of the inverse water-gas shift reaction mixture and heating to about 300 °C for LSF results in a readsorption of hydrogen between ∼300 and ∼470 °C, without simultaneously observing inverse water-gas shift reactivity. Only above ∼470 °C, the i-WGS reaction sets in. A similar behavior, albeit at slightly different temperatures and less pronounced, is also observed for STF (Figure 6E). In order to determine the rate-limiting step of the reaction, thus the depth of reduction in the active working state of the catalysts and the associated specific reactivity of the reduced centers at the surface has to be considered. These appear clearly different from those obtained after prereduction of a fully oxidized sample. In this respect, the water-gas shift reaction on fully oxidized perovskite samples only yields total oxidation to $CO_2$ (cf. Figure S4).

Comparative experiments on the methane reactivity clearly indicate that on fully oxidized catalyst samples in the absence of water as well as under steam reforming conditions methane is always totally oxidized to $CO_2$; the corresponding catalytic results are depicted in Figure 6, panels C and G, as well as in Figure S5 of the Supporting Information, respectively. Most importantly, on prereduced perovskite catalysts ($H_2$, 600 °C, 1 h) no methane reactivity at all was observed under otherwise comparable experimental conditions (cf. Supporting Information Figure S6). This indicates that the fully oxidized states of LSF and STF exhibit reactive oxygen species capable of fully oxidizing methane—in contrast to a deeply reduced state, where the remaining oxygen species obviously are unreactive toward methane. Hence, also no methane reforming activity is observed. Especially for LSF, partial reoxidation by water has been observed (see cf. Figure 4), which is anyway not enough to set in methane oxidation. This can be understood on the basis that water obviously dissociatively adsorbs on the surface through partial refilling of vacancies. As this does not lead to methane reactivity, we might infer that methane reactivity is hindered because of missing methane activation. This might be partially connected to the iron content of the sample and the associated redox chemistry (cf. Figure S4).

The results on methane oxidation are in good agreement with reports by Belessi for the reaction of CO and NO[26] and Spinicci et al. for the total oxidation of methane using $LaFeO_3$, who observed a significant influence of the nonstoichiometry on the activity between compositions of $La_{0.95}FeO_{2.85}$ and $La_{0.7}FeO_{2.55}$.[22] (Partial) oxidation of methane is generally a reaction that has been vastly studied on many different perovskite systems,[53−58] but almost always using a chemical looping pulse technique at higher reaction temperatures. Summarizing—in close correlation to the results presented here—oxygen nonstoichiometry has been elucidated as the key parameter governing the activity and stability. However, structure−activity correlations appear scarce especially regarding reforming reactions, and research is therefore focused on methane combustion. It is clear, nevertheless, that upon presence of water the complexity is much higher and qualitative differences in the oxygen vacancies between perovskite systems may arise—as can be seen in Figures 4 and 6.

**3.3. Structural Characterization.** For establishment of unambiguous structure−activity correlations, a clear picture of structural and morphological changes occurring upon catalyst pretreatments as well as during reaction must evolve. This is even more imperative given the complexity of the perovskite systems under investigation. In due course, the catalysts were characterized by electron microscopy, X-ray diffraction, and Raman spectroscopy after each step of a full inverse water-gas shift reaction cyle including preoxidation and prereduction. Scanning high-resolution transmission electron microscopy was used to determine the surface termination of both perovskites to detect eventual irreversible structural changes in the catalytically relevant surface regions. X-ray diffraction and Raman spectroscopy were then used to investigate perovskite lattice stability and to eventually corroborate the above-discussed TPR profiles, especially regarding the influence of prereduction. This in due course also raises the question of full reversibility of the changes introduced both by the specific pretreatments and the subsequent catalytic reaction. In order to serve as a valuable (electro)catalyst, all structural changes must be fully reversible upon reoxidation after reduction and reaction. Especially for more complex systems, this is by no means a trivial question and needs to be accurately assessed.

*3.3.1. Transmission Electron Microscopy.* Figure 7 highlights the morphology of a representative STF grain in the as-grown state (corresponding high-resolution TEM images are



DOI: 10.1021/acs.jpcc.5b02947
J. Phys. Chem. C 2015, 119, 11739−11753

highlighted in Figure S7 of the Supporting Information). Panel A shows a bright-field transmission electron microscopy (TEM) image of a micrometer-sized grain with some internal structure being mostly due to mass−thickness contrast, whereas panel B reveals that STF is basically chemically homogeneous after the catalytic reaction and no pronounced chemical segregation takes place. For this purpose, the corresponding Ti−K (a), Fe−K (b), Sr−L (c), and O−K edges are mapped over the indicated squared region by energy-dispersive X-ray spectroscopy (EDX). Before performing the EDX experiments, a high-angle annular dark-field (HAADF) image of the grain was taken, which also shows no substantial variation in chemical composition. Note that the HAADF contrast is basically proportional to $Z^2$ (with $Z$ denoting the atom number), thickness $t$, and material density $\rho$. Thus, regions with greater $Z$ or higher thickness appear brighter in the corresponding images. By combination of HAADF images and EDX measurements, the contrast variations in the former image are clearly only due to thickness variations.

To further shed light on the structural changes on the atomic level during each step of a catalytic cycle, (scanning) high-resolution electron microscopy imaging was performed for visualizing changes in the ordering of the samples, but most importantly, for changes in the bulk structure and surface termination.

The corresponding surface termination after performing the active inverse water-gas shift state is subsequently shown in the atomically resolved STEM-HAADF images of Figure 8 (panel A, STF; panel B, LSF). Ball models of the respective structures are shown as large insets, with the different colors denoting the different atoms present in the structures. Furthermore, due to the resolved atom rows, it is possible to assign the individual atoms to the intensity profile in the HAADF image. It should be noted that, despite difficulties to distinguish Fe from Ti and Sr from La, the A and the B cations can clearly be distinguished. The Sr atoms, as the heaviest atoms, appear correspondingly bright in these images. Thus, the surfaces can clearly identified to be predominantly (Sr,La)O-terminated after the catalytic run, and no Fe/Ti segregation was observed for any of the perovskite structures. In Figure 8, panel B, the (Sr,La)O termination of the LSF surface is best visible at the bottom left side, where a side edge of the crystallite is shown. These results are in line with recent results on the surface composition of LSF in different gas atmospheres, obtained by *in situ* X-ray photoelectron spectroscopy studies, which also strongly indicate a Sr−O termination of the surface.[70]

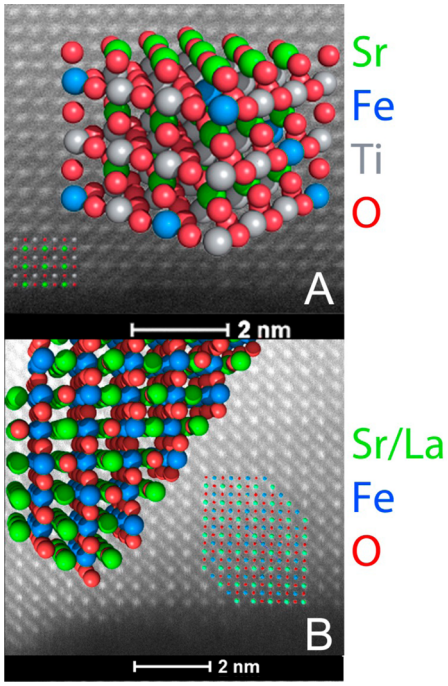


**Figure 8.** High-resolution STEM-HAADF images of STF (above) and LSF (below) with ball models of both crystallographic structures as overlayers to visualize the exact position of each atom in the structure and at the surface.

*3.3.2. X-ray Diffraction.* X-ray diffraction has already been shown to be a valuable tool to investigate the bulk structural changes of several perovskite systems, especially regarding changes in crystallite size, lattice parameters, oxygen vacancy concentration, or valence state as well as structural transformations upon oxidative and reductive treatments at elevated temperatures.[60−62,80] In due course, we will show if and how the bulk structure is affected by the reductive or catalytic (pre)treatments.

Figure 9 summarizes the obtained XRD patterns on STF and LSF powder samples. The red diffractogram in panel A, corresponding to the initial, untreated sample, is in agreement with the cubic structure of $SrFe_{1-x}Ti_xO_3$ reported e.g. by Adler et al., whose structure data can be used as starting values for refining.[90] The obtained lattice parameter of $a$ = 3.899 Å (from fitting of the peaks including the split peaks of $K\alpha_1$ and $K\alpha_2$ at

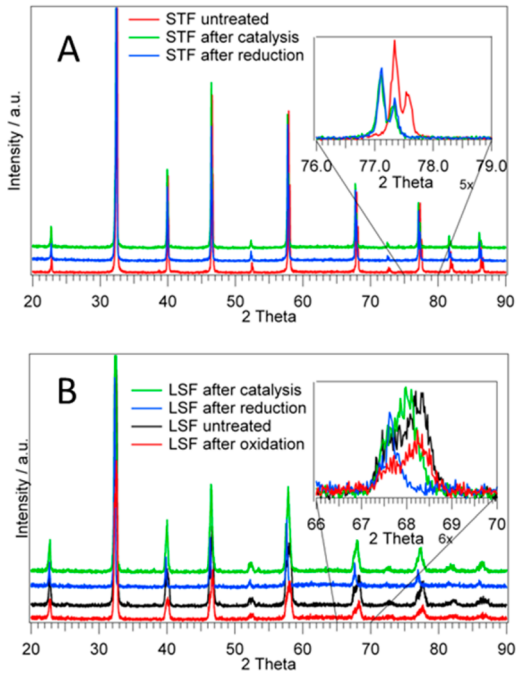


**Figure 9.** (A) X-ray diffraction patterns of STF collected after different steps of a catalytic cycle. Initial state (red), after reduction at 600 °C in 1 bar of hydrogen (blue) and after catalysis as described before (i-WGSR, green). The inset shows a close-up view of the peaks at around $2\theta$ = 77°. (B) X-ray diffraction patterns of LSF collected after different steps of a catalytic cycle. Initial state (black), after reduction at 600 °C in 1 bar of hydrogen (blue), after i-WGSR (green) and after reoxidation at 400 °C in 1 bar of oxygen (red). The inset shows a close-up view of the peaks at around $2\theta$ = 68°.



DOI: 10.1021/acs.jpcc.5b02947
J. Phys. Chem. C 2015, 119, 11739−11753

higher angles—see also the inset) corroborates this conclusion. After reduction, however, a significant shift of the peaks to lower diffraction angles is observed, which can be most clearly seen in the inset highlighting the group of peaks around $2\theta$ = 77°. This shift has also been observed previously and has, in combination with XANES spectra, been assigned to formation of oxygen vacancies and the corresponding changes in the Fe valence state, both causing a change in the lattice parameter.[61] Most notably, as highlighted in the green XRD pattern, this shift is not reversed during prolonged contact to the inverse water-gas shift reaction mixture but can only be reversed by reoxidative treatment at 400 °C (see also the corresponding Raman spectroscopy experiments in the following section). For LSF the XRD experiments show a very similar behavior as can be seen by comparing the red and black XRD pattern in Figure 9, panel B, denoting the initial state and the state after final reoxidation at 400 °C with oxygen, respectively. The initial diffractogram (black) again corresponds well to literature-reported data on the rhombohedral $Sr_{0.4}La_{0.6}FeO_{2.8}$ structure.[62] Using $CO/CO_2$ mixtures of varying content, corresponding to different reduction potentials, a slight shift of the peaks as well as a corresponding intensity increase of the peak at lower $2\theta$ was observed with increasing CO content.[62] In our case, the same features are observed: the intensity of the peak at higher $2\theta$ (at 68.4°) cannot be distinguished from the background noise upon reduction (blue trace) but more or less re-established after the catalytic reaction (green trace) and after reoxidation.

In summary, also the XRD experiments allowed for monitoring the structural changes after each step of the catalytic cycle and yielded direct information with respect to the formation and reactivity of oxygen vacancies after the prereduction procedures. Our XRD experiments also corroborated the above-mentioned differences between STF and LSF with respect to the reactivity of oxygen vacancies toward water (cf. Figure 4). The changes introduced by STF prereduction could not be reversed by either water formed during catalytic reaction or a direct treatment but only by reoxidation in molecular oxygen. In contrast, in the case of LSF the initial state is almost re-established even by water formed during the catalytic reaction (and even more by a direct treatment, cf. Figure 4). Consequently, this again implies a different extent of reduction of STF and LSF under comparable reaction conditions and also the presence of more reactive defects toward $H_2O$ in the case of LSF.

*3.3.3. Raman Spectroscopy.* Raman spectroscopy has already been proven to be an indispensable tool to characterize the structure of various perovskites, including STF and LSF, not only in the initial state but also after various annealing treatments.[61,91−93] Moreover, the Raman spectrum of the archetypical $SrTiO_3$ perovskite is already well-understood, as are the effects of temperature, grain boundaries, and sizes or phase transitions.[91,93,94] STF and LSF have also been characterized regarding the effects of anodic or cathodic polarization or charge-disproportionation phase transitions.[93] Hence, as the method is already well-established and a sufficiently large data set is already available, it is a promising methodical approach to study the catalytic effects on the structure of the perovskite systems described in the preceding sections. The experiments have been in this case restricted to the STF material, as LSF shows pronounced luminescence effects, rendering the measurements of real Raman shifts difficult.

In close correlation to the other experiments, Figure 10 now summarizes the Raman spectra acquired after different steps of

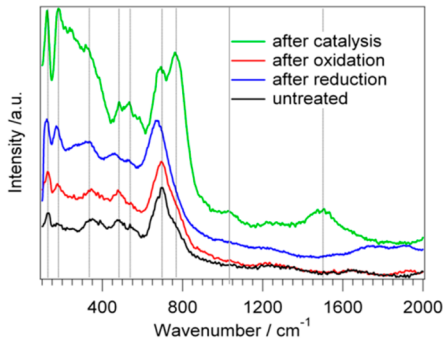


**Figure 10.** Raman spectra collected on STF after various catalytic treatments: black, untreated sample; blue, after reduction at 600 °C in hydrogen (1 h); red, after reoxidation at 400 °C (1 h); green, after i-WGSR up to 600 °C (1 h). Spectra are shifted upward for more clarity. Vertical lines have been added to distinct features as a guide to the eye.

catalyst pretreatment and reaction. The black spectrum refers to the initial, untreated STF perovskite, which in due course will be used as reference material for all structural changes. For full appreciation of the spectral changes, it is useful to give a brief overview of the Raman spectrum of the untreated STF state. The spectrum between 200 and 2000 $cm^{-1}$ reveals several pronounced peaks at 125, 180, 325, 480, 540, and 770 $cm^{-1}$ and a number of very broad signals above 1000 $cm^{-1}$. Except the one at 700 $cm^{-1}$, these correspond (with increasing wavenumber) to the TO1, LO1/TO2, LO2/TO3, LO3, TO4, and LO4 transversal and longitudinal optical phonon modes, respectively.[61] Most importantly, the LO4 mode at 770 $cm^{-1}$ is hardly present in the spectrum of untreated STF. The most pronounced feature at 700 $cm^{-1}$ and the associated shoulder at LO4 770 $cm^{-1}$ have been observed by Vracar et al. to be strongly affected by variations in the iron content of the sample.[61] The latter was found to be very pronounced for low iron contents but getting progressively weaker in relation to the feature at 700 $cm^{-1}$ with increasing iron content. Hence, peak shifts or intensity variations of these peaks might be used as an indicator for local changes in the structural environment of Fe-containing centers.

After reduction at 600 °C in hydrogen (blue spectrum) the overall features do not change substantially, with the one exception of an even more suppressed intensity of the LO4 mode at 770 $cm^{-1}$. However, after the catalytic reaction (green spectrum), the changes are much more pronounced. This basically refers to intensity changes of the TO4 and LO4 modes and to the appearance of several new peaks, especially in the high wavenumber region. New features are now found at 1050 and 1500 $cm^{-1}$, and the LO4 mode, previously only present as a suppressed shoulder, has now gained intensity and exceeds the corresponding TO4 mode. The LO4 mode itself corresponds to a Ti−O or a Fe−O stretching vibration[91] and is connected with the features at 1050 and 1500 $cm^{-1}$. The peak at 1500 $cm^{-1}$ (a 2LO4 overtone) gains only intensity, if the associated LO4 mode gets progressively more pronounced. The peak at 1050 $cm^{-1}$ most probably is a superposition of the overtones of the 2LO2 and 2TO4 modes.[91] Note also the pronounced peak shift between the spectrum of the untreated perovskite and the reduced state, which is practically reversed upon treatment in the catalytic inverse water-gas shift reaction


DOI: 10.1021/acs.jpcc.5b02947
J. Phys. Chem. C 2015, 119, 11739−11753

mixture. After reoxidation at 400 °C (red spectrum), all previously introduced changes are completely reversed and the initial state is clearly re-established. Taking the XRD result into consideration, the following correlation arises: from the XRD measurements after prereduction, the creation of an increasing number of oxygen vacancies has been inferred after reduction, which is now accompanied by the almost total suppression of the LO4 mode and the red-shifted peaks. After catalysis, the XRD measurements did not indicate reversal of the bulk structural changes introduced by the reduction but showed that the inverse water-gas shift reaction atmosphere is not able to fully replenish especially the bulk vacancies. In contrast, the Raman experiments after catalysis show that part of the introduced changes can be indeed reversed, as indicated by the shift of LO4 peak position back to the "oxidized" state (note, however, that there are still some differences between the Raman spectra of the untreated and "oxidized" STF sample, which indicate that some irreversible structural changes are still present). Most importantly, as the changes in the spectrum mainly affect the peaks sensitive to the Fe content, we might conclude that these changes not only mainly affect surface-near regions but also appear to be at least in part associated with a local concentration change of Fe-containing centers. Although the STEM images showed that these changes obviously do not alter the surface termination of STF, we nevertheless may assume that the STF surface-near regions are in a highly dynamic state, adapting easily to the reductive or oxidative environments of catalyst pretreatment or reaction.

## 4. CONCLUSIONS

In the present study the (electro)catalytic properties of the reducible perovskite-type oxides $La_{0.6}Sr_{0.4}FeO_{3-\delta}$ and $SrTi_{0.7}Fe_{0.3}O_{3-\delta}$ were investigated. The activity of LSF for the (electro)oxidation of hydrogen was studied by means of impedance spectroscopy experiments on model-type thin film electrodes. Interestingly, the surface resistance (which is a measure of the surface activity) at ca. 610 °C in a $H_2/H_2O$ atmosphere was very similar to the surface resistance in synthetic air. Compared to STF, the activity of LSF for the $H_2$ oxidation reaction is significantly higher. Catalytic-wise, the presented results allow the correlation of a catalytic profile measured on a perovskite system to bulk and surface structural changes occurring during each step of catalytic pretreatments and catalytic reaction. For this correlation two different types of experiments were necessary:

(1) Catalytic measurements identifying the activity of the perovskite-type catalysts. Exemplarily shown for the inverse water-gas shift equilibrium, a pretreatment of the perovskite powders in hydrogen is a prerequisite for a successful use of LSF and STF as WGSR catalysts. Using this pretreatment and combining XRD and catalytic experiments (for STF also Raman measurements), a clear difference in the surface and bulk reactivity of the two perovskite-type oxides was unveiled. Thus, as the most important parameter highly influencing the reactivity, the reduction degree and depth could be determined: it controls the oxygen reactivity and the specific oxidation and reduction capability of the active sites in the working state of the catalysts. Especially, the methane activation/oxidation ability strongly depends on the chosen reduction depth.

(2) By means of high-resolution TEM measurements on both catalyst powders a predominant SrO—or (Sr,La)O—surface termination could be verified after a catalytic reaction, indicating that a bulk-proportional surface contribution of e.g. redox-active iron centers in both catalysts is unlikely and a more complex scenario, especially with regard to qualitatively differently oxygen-affine surface-near vacancies and a reaction- and segregation-specific concentration of such redox-active sites at the surface, must be assumed.

## ■ ASSOCIATED CONTENT

### Supporting Information

SEM image of a circular 200 nm thick LSF electrode with buried Ti/Pt grid (Figure S1); schematics of the thin film electrode system (Figure S2, adapted from ref 69); temperature-dependent water-gas shift equilibrium for the chosen experimental conditions (Figure S3); temperature-programmed water-gas shift reaction on fully oxidized perovskite samples (Figure S4); temperature-programmed methane steam reforming on fully oxidized perovskite samples (Figure S5); temperature-programmed methane steam reforming on prereduced perovskite samples (Figure S6); high-resolution TEM images of STF in [001] orientation (panel A) and LSF in [001] orientation (panel B) after the catalytic i-WGSR reaction (Figure S7). The Supporting Information is available free of charge on the ACS Publications website at DOI: 10.1021/acs.jpcc.5b02947.

## ■ AUTHOR INFORMATION

### Corresponding Author

*(S.P.) Tel 004351250758003; Fax 004351250758198; e-mail simon.penner@uibk.ac.at.

### Notes

The authors declare no competing financial interest.

## ■ ACKNOWLEDGMENTS

We thank the FWF (Austrian Science Foundation) for financial support under the projects FOXSI F4503 and F4509. We are indebted to R. Kaindl for valuable discussion of the Raman spectra.

## ■ ADDITIONAL NOTE

[a]Please note that in air the part of the LSF surface above the current collecting mesh is not electrochemically active owing to the low ionic conductivity of LSF at this $p(O_2)$. However, under reducing conditions the entire surface area is expected to be electrochemically active despite the presence of the buried current collectors at the interface due to the relatively high ionic conductivity of LSF. Here, an explanation of details would be far beyond the scope of the present paper—thus the interested reader is referred to a more detailed study on LSF[79] and to a mechanistic study on STF electrodes with geometrically well-defined current collectors.[43]

## ■ REFERENCES

(1) Rodriguez, J. A.; Fernandez-Garcia, M. *Synthesis, Properties and Applications of Oxide Nanomaterials*; Wiley Interscience: New York, 2007.

(2) Henrich, V. E.; Cox, P. A. *The Surface Chemistry of Metal Oxides*; Cambridge University Press: Cambridge, UK, 1994.

(3) Noguera, C. *Physics and Chemistry at Oxide Surfaces*; Cambridge University Press: Cambridge, UK, 1996.

(4) Wachs, I. E. Recent Conceptual Advances in the Catalysis Science of Mixed Metal Oxide Catalytic Materials. *Catal. Today* **2005**, *100*, 79−94.



DOI: 10.1021/acs.jpcc.5b02947
J. Phys. Chem. C 2015, 119, 11739−11753

(5) Lopez-Nieto, J. M.; Botella, P.; Solsona, B.; Oliver, J. M. The Selective Oxidation of Propane on Mo-V-Te-Nb-O Catalysts: The Influence of Te-Precursor. *Catal. Today* **2003**, *81*, 87−94.
(6) Guliants, V. V.; Benziger, J. B.; Sundaresan, S.; Yao, N.; Wachs, I. E. Evolution of the Active Surface of the Vanadyl Pyrophosphate Catalysts. *Catal. Lett.* **1995**, *32*, 379−386.
(7) Freeman, D.; Wells, R. P. K.; Hutchings, G. J. Conversion of Methanol to Hydrocarbons over $Ga_2O_3$/H-ZSM-5 and $Ga_2O_3/WO_3$ Catalysts. *J. Catal.* **2002**, *205*, 358−365.
(8) Lopez-Nieto, J. M.; Botella, P.; Vazquez, M. I.; Dejoz, A. The Selective Oxidative Dehydrogenation of Ethane over Hydrothermally Synthesised MoVTeNb Catalysts. *Chem. Commun.* **2002**, *7*, 1906−1907.
(9) Yao, W. F.; Xu, X. H.; Zhou, J. T.; Yang, X. N.; Zhang, Y.; Shang, S. X.; Wang, H.; Huang, B. B. Photocatalytic Property of Sillenite $Bi_{24}AlO_{39}$ Crystals. *J. Mol. Catal. A: Chem.* **2004**, *212*, 323−328.
(10) Hävecker, M.; Knop-Gericke, A.; Mayer, R. W.; Fait, M.; Bluhm, H.; Schlögl, R. Influence of the Geometric Structure on the V L3 Near Edge X-ray Absorption Fine Structure from Vanadium Phosphorus Oxide Catalysts. *J. Electron Spectrosc. Relat. Phenom.* **2002**, *125*, 79−87.
(11) Mashkina, E.; Magerl, A.; Ollivier, J.; Göbbels, M.; Seifert, F. Oxygen Mobility in the Perovskite $SrTi_{1-x}Fe_xO_{3(x=0.8)}$. *Phys. Rev. B* **2006**, *74*, 214106-1−214106-7.
(12) Buttner, R. H.; Maslen, E. N. Structural Parameters and Electron Difference Density in $BaTiO_3$. *Acta Crystallogr., Sect. B* **1992**, *48*, 764−769.
(13) Wesche, R. *High-Temperature Superconductors − Materials, Properties and Applications*; Kluwer: Boston, 1998.
(14) Adler, S. B. Factors Governing Oxygen Reduction in Solid Oxide Fuel Cell Cathodes. *Chem. Rev.* **2004**, *104*, 4791−4843.
(15) Dacquin, J. P.; Lancelot, C.; Dujardin, C.; Cordier-Robert, C.; Granger, P. Support-Induced Effects of $LaFeO_3$ Perovskite on the Catalytic Performances of Supported Pt Catalysts in DeNOx Applications. *J. Phys. Chem. C* **2011**, *115*, 1911−1921.
(16) Pecchi, G.; Delgado, E. J. Perovskites as Catalysts for Environmental Remediation. *Perovskite* **2013**, 97−116.
(17) Villoria, J.-A.; Mota, N.; Al-Sayari, S. A.; Alvarez-Galvan, M.-C.; Navarro, R.-M.; Fierro, J. L. G. Perovskites as Catalysts in the Reforming of Hydrocarbons: A Review. *Micro Nanosyst.* **2012**, *4*, 231−252.
(18) Eyssler, A.; Lu, Y.; Matam, S. K.; Weidenkaff, A.; Ferri, D. Perovskite-Supported Palladium for Methane Oxidation - Structure-Activity Relationships. *Chimia* **2012**, *66*, 675−680.
(19) Yoon, J. S.; Lim, Y. S.; Choi, B. H.; Hwang, H. J. Catalytic Activity of Perovskite-Type Doped $La_{0.08}Sr_{0.92}Ti_{1-x}M_xO_{3-\delta}$ (M = Mn, Fe, and Co) Oxides for Methane Oxidation. *Int. J. Hydrogen Energy* **2014**, *39*, 7955−7962.
(20) Zhao, Z.; Dai, H.; Deng, J.; Du, Y.; Liu, Y.; Zhang, L. Three-Dimensionally Ordered Macroporous $La_{0.6}Sr_{0.4}FeO_{3-\delta}$: High-Efficiency Catalysts for the Oxidative Removal of Toluene. *Microporous Mesoporous Mater.* **2012**, *163*, 131−139.
(21) Abe, K.; Fukunaga, T. Eur. Pat. Appl. 14pp., Patent, 1990.
(22) Spinicci, R.; Tofanari, A.; Delmastro, A.; Mazza, D.; Ronchetti, S. Catalytic Properties of Stoichiometric and Non-Stoichiometric $LaFeO_3$ Perovskite for Total Oxidation of Methane. *Mater. Chem. Phys.* **2002**, *76*, 20−25.
(23) Martinez-Ortega, F.; Batiot-Dupeyrat, C.; Valderrama, G.; Tatibouet, J. M. Methane Catalytic Combustion on La-Based Perovskite Catalysts. *Chemistry* **2001**, *49*, 49−55.
(24) Lima, S. M.; Assaf, J. M.; Pena, M. A.; Fierro, J. L. G. Structural Features of $La_{1-x}Ce_xNiO_3$ Mixed Oxides and Performance for the Dry Reforming of Methane. *Appl. Catal., A* **2006**, *311*, 94−104.
(25) Wang, Y.; Wang, X.; Lu, L.; Wang, X. Experimental Study on Preparation of $LaMO_3$ (M = Fe, Co, Ni) Nanocrystals and Their Catalytic Activity. *Thermochim. Acta* **2006**, *443*, 225−230.
(26) Belessi, V. C.; Trikalitis, P. N.; Ladavos, A. K.; Bakas, T. V.; Pomonis, P. Structure and Catalytic Activity of $La_{1-x}FeO_3$ System ($x$ = 0.00, 0.05, 0.10, 0.15, 0.20, 0.25, 0.35) for the NO + CO Reaction. *J. Appl. Catal.* **1999**, *177*, 53−68.
(27) Kwak, J. N.; Lee, S. G.; Lee, S. H.; Park, Y.; Sohn, J. The Study on the Catalytic Performance and Characterization of Perovskite Catalyst ($La_{0.9}Sr_{0.1}Cr_{1-2x}Mn_xCo_xO_{3\pm\delta}$) for High Temperature Water−Gas Shift Reaction with Simulated Coal-Derived Syngas. *Catal. Today* **2014**, *232*, 11−15.
(28) Sun, E. Y.; Hla, S. S.; Duffy, G. J.; Cousins, A. J.; French, D.; Morpeth, L. D.; Edwards, J. H.; Roberts, D. G. Effect of Ce on the Structural Features and Catalytic Properties of $La_{(0.9-x)}Ce_xFeO_3$ Perovskite-Like Catalysts for the High Temperature Water-Gas Shift Reaction. *Int. J. Hydrogen Energy* **2011**, *36*, 79−86.
(29) Ma, H.; Zhu, H.; Tan, X.; Zhang, J. Preparation and High-Temperature Water-Gas Shift Catalytic Features of $La_{1-x}Ce_x$ $FeO_3$ Perovskite. *J. Rare Earths* **2004**, *22*, 357−360.
(30) Pena, M. A.; Fierro, J. L. G. Chemical Structures and Performance of Perovskite Oxides. *Chem. Rev.* **2001**, *101*, 1981−2017.
(31) Royer, S.; Duprez, D.; Can, F.; Courtois, X.; Batiot-Dupeyrat, C.; Lassiri, S.; Alamdari, H. Perovskites as Substitutes of Noble Metals for Heterogeneous Catalysis: Dream or Reality. *Chem. Rev.* **2014**, *114*, 10292−10368.
(32) Cho, S.; Fowler, D. E.; Miller, E. C.; Cronin, J. S.; Poeppelmeier, K. R.; Barnett, S. A. Fe-Substituted $SrTiO_{3-\delta}$-$Ce_{0.9}Gd_{0.1}O_2$ Composite Anodes for Solid Oxide Fuel Cells. *Energy Environ. Sci.* **2013**, *6*, 1850−1857.
(33) Tao, S.; Irvine, J. T. S. Synthesis and Characterization of $(La_{0.75}Sr_{0.25})Cr_{0.5}Mn_{0.5}O_{3-\delta}$, a Redox-Stable, Efficient Perovskite Anode for SOFCs. *J. Electrochem. Soc.* **2004**, *151*, A252−A259.
(34) Cowin, P. I.; Petit, C. T. G.; Lan, R.; Irvine, J. T. S.; Tao, S. Recent Progress in the Development of Anode Materials for Solid Oxide Fuel Cells. *Adv. Energy Mater.* **2011**, *1*, 314−332.
(35) Tao, S.; Irvine, J. T. S. Catalytic Properties of the Perovskite Oxide $La_{0.75}Sr_{0.25}Cr_{0.5}Fe_{0.5}O_{3-\delta}$ in Relation to Its Potential as a Solid Oxide Fuel Cell Anode Material. *Material. Chem. Mater.* **2004**, *16*, 4116−4121.
(36) *High Temperature Solid Oxide Fuel Cells: Fundamentals, Design and Applications*; Singhal, S. C., Kendall, K., Eds.; Elesvier: Amsterdam, 2003.
(37) Patrakeev, M. V.; Bahteeva, J. A.; Mitberg, E. B.; Leonidov, I. A.; Kozhevnikov, V. L.; Poeppelmeier, K. R. Electron/Hole and Ion Transport in $La_{1-x}Sr_xFeO_{3-\delta}$. *J. Solid State Chem.* **2003**, *172*, 219−231.
(38) Kuhn, M.; Hashimoto, S.; Sato, K.; Yashiro, K.; Mizusaki, J. Oxygen Nonstoichiometry, Thermo-Chemical Stability and Lattice Expansion of $La_{0.6}Sr_{0.4}FeO_{3-\delta}$. *Solid State Ionics* **2011**, *195*, 7−15.
(39) Aljaberi, A. D.; Irvine, J. T. S. Ca-Substituted, A-Site Deficient Perovskite $La_{0.2}Sr_{0.7}TiO_3$ as a Potential Anode Material for SOFCs. *J. Mater. Chem. A* **2013**, *1*, 5868−5874.
(40) Wedig, A.; Lynch, M. E.; Merkle, R.; Maier, J.; Liu, M. Sheet Resistance in Thin Film Solid Oxide Fuel Cell Model Cathodes: A Case Study on Circular $Bi_{1-x}Sr_xFeO_{3-\delta}$ Microelectrodes. *ECS Trans.* **2012**, *45*, 213−224.
(41) Opitz, A. K.; Kubicek, M.; Huber, S.; Huber, T.; Holzlechner, G.; Hutter, H.; Fleig, J. Thin Film Cathodes in SOFC Research: How To Identify Oxygen Reduction Pathways? *J. Mater. Res.* **2013**, *28*, 2085−2105.
(42) Chueh, W. C.; Hao, Y.; Jung, W.; Haile, S. M. High Electrochemical Activity of the Oxide Phase in Model Ceria−Pt and Ceria−Ni Composite Anodes. *Nat. Mater.* **2012**, *11*, 155−161.
(43) Nenning, A.; Opitz, A. K.; Huber, T.; Fleig, J. A Novel Approach for Analyzing Electrochemical Properties of Mixed Conducting Solid Oxide Fuel Cell Anode Materials by Impedance Spectroscopy. *Phys. Chem. Chem. Phys.* **2014**, *16*, 22321−22336.
(44) Huang, Y.; Dass, R. I.; Xing, Z.; Goodenough, J. B. Double Perovskites as Anode Materials for Solid-Oxide Fuel Cells. *Science* **2006**, *312*, 254−257.
(45) Mai, A.; Haanappel, V.; Uhlenbruck, S.; Tietz, F.; Stöver, D. Ferrite-Based Perovskites as Cathode Materials for Anode-Supported Solid Oxide Fuel Cells: Part I. Variation of Composition. *Solid State Ionics* **2005**, *176*, 1341−1350.


DOI: 10.1021/acs.jpcc.5b02947
*J. Phys. Chem. C* 2015, 119, 11739−11753

(46) Yamamoto, O.; Takeda, Y.; Kanno, R.; Noda, M. Perovskite-Type Oxides as Oxygen Electrodes for High Temperature Oxide Fuel Cells. *Solid State Ionics* **1987**, *22*, 241−246.
(47) *Functional Materials For Sustainable Energy Applications*; Kilner, J., Skinner, S., Irvine, S., Edwards, P., Eds.; Woodhead Publishing Series in Energy; Woodhead Publishing Limited: Cambridge, 2012.
(48) Zhang, Y.; Chen, C.; Lin, X.; Li, D.; Chen, X.; Zhan, Y.; Zheng, Q. $CuO/ZrO_2$ Catalysts for Water-Gas Shift Reaction: Nature of Catalytically Active Copper Species. *Int. J. Hydrogen Energy* **2014**, *39*, 3746−3756.
(49) Tanaka, Y.; Utaka, T.; Kikuchi, R.; Takeguchi, T.; Sasaki, K.; Eguchi, K. Water Gas Shift Reaction for the Reformed Fuels over Cu/MnO Catalysts Prepared via Spinel-Type Oxide. *J. Catal.* **2003**, *215*, 271−278.
(50) Daza, Y. A.; Maiti, D.; Kent, R. A.; Bhethanabotla, V. R.; Kuhn, J. N. Isothermal Reverse Water Gas Shift Chemical Looping on $La_{0.75}Sr_{0.25}Co_{(1-Y)}Fe_YO_3$ Perovskite-Type Oxides. *Catal. Today* **2015**, DOI: 10.1016/j.cattod.2014.12.037.
(51) Dai, X. P.; Wu, Q.; Li, R. J.; Yu, C. C.; Hao, Z. P. Hydrogen Production from a Combination of the Water−Gas Shift and Redox Cycle Process of Methane Partial Oxidation via Lattice Oxygen over $LaFeO_3$ Perovskite Catalyst. *J. Phys. Chem. B* **2006**, *110*, 25856−25862.
(52) Daza, Y. A.; Kent, R. A.; Yung, M. M.; Kuhn, J. N. Carbon Dioxide Conversion by Reverse Water-Gas Shift Chemical Looping on Perovskite-Type Oxides. *Ind. Eng. Chem. Res.* **2014**, *53*, 5828−5837.
(53) Rajesh, T.; Devi, R. N. Role of Oxygen Vacancies in Water Gas Shift Reaction: Activity Study on $BaCe_{0.98-x}Y_xPt_{0.02}O_{3-\delta}$ Perovskites. *J. Phys. Chem. C* **2014**, *118*, 20867−20874.
(54) Gallego, G. S.; Batiot-Dupeyrat, C.; Mondragon, F. Methane Partial Oxidation by the Lattice Oxygen of the $LaNiO_{3-\delta}$ Perovskite. A Pulse Study. *Dyna* **2010**, *163*, 141−150.
(55) Kharton, V. V.; Patrakeev, M. V.; Waerenborgh, J. C.; Sobyanin, V. A.; Veniaminov, S. A.; Yaremchenko, A. A.; Frade, J. R. Methane Oxidation over Perovskite-Related Ferrites: Effects of Oxygen Nonstoichiometry. *Solid State Sci.* **2005**, *7*, 1344−1352.
(56) Mihai, O.; Chen, D.; Holmen, A. Catalytic Consequence of Oxygen of Lanthanum Ferrite Perovskite in Chemical Llooping Reforming of Methane. *Ind. Eng. Chem. Res.* **2011**, *50*, 2613−2621.
(57) Gao, Z.; Wang, R. Catalytic Activity for Methane Combustion of the Perovskite-Type $La_{1-x}Sr_xCoO_{3-\delta}$ Oxide Prepared By the Urea Decomposition Method. *Appl. Catal., B* **2010**, *98*, 147−153.
(58) Murugan, A.; Thursfield, A.; Metcalfe, I. S. A Chemical Looping Process for Hydrogen Production Using Iron-Containing Perovskites. *Energy Environ. Sci.* **2011**, *4*, 4639−4649.
(59) Tanaka, Y.; Utaka, T.; Kikuchi, R.; Takeguchi, T.; Sasaki, K.; Eguchi, K. Water Gas Shift Reaction over Cu-Based Mixed Oxides for CO Removal from the Reformed Fuels. *Appl. Catal., A* **2003**, *242*, 287−295.
(60) Kuhn, M.; Hashimoto, S.; Sato, K.; Yashiro, K.; Mizusaki, J. Oxygen Nonstoichiometry, Thermo-Chemical Stability and Lattice Expansion of $La_{0.6}Sr_{0.4}FeO_{3-\delta}$. *Solid State Ionics* **2011**, *195*, 7−15.
(61) Vracar, M.; Kuzmin, A.; Merkle, R.; Prans, J.; Kotomin, E. A.; Maier, J.; Mathon, O. Jahn-Teller Distortion around $Fe^{4+}$ in $Sr(Fe_xTi_{1-x})O_{3-\delta}$ from X-ray Absorption Spectroscopy, X-ray Diffraction, and Vibrational Spectroscopy. *Phys. Rev. B* **2007**, *76*, 174107−1−174107−11.
(62) Yang, J. B.; Yelon, W. B.; James, W. J.; Chu, Z.; Kornecki, M.; Xie, Y.; Zhou, X.; Anderson, H. U.; Joshi, A.; Malik, S. Crystal Structure, Magnetic Properties, and Mössbauer Studies of $La_{0.6}Sr_{0.4}FeO_{3-\delta}$ Prepared by Quenching in Different Atmospheres. *Phys. Rev. B* **2002**, *66*, 184415−1−184415−9.
(63) Chen, Y.; Jung, W.; Cai, Z.; Kim, J.; Tuller, H.; Yildiz, B. Impact of Sr Segregation on the Electronic Structure and Oxygen Reduction Activity of $SrTi_{1-x}Fe_xO_3$ Surfaces. *Energy Environ. Sci.* **2012**, *5*, 7979−7988 and references therein.
(64) Szot, K.; Pawelczyk, M.; Herion, J.; Freiburg, C.; Albers, J.; Waser, R.; Hulliger; Kwapulinski, J. J.; Dec, J. Nature of the Surface Layer in $ABO_3$-Type Perovskites at Elevated Temperatures. *Appl. Phys. A: Mater. Sci. Process.* **1996**, *62*, 335−343.
(65) Fister, T. T.; Fong, D. D.; Eastman, J. A.; Baldo, P. M.; Highland, M. J.; Fuoss, P. H.; Balasubramaniam, K. R.; Meador, J. C.; Salvador, P. A. In Situ Characterization of Strontium Surface Segregation in Epitaxial $La_{0.7}Sr_{0.3}MnO_3$ Thin Films as a Function of Oxygen Partial Pressure. *Appl. Phys. Lett.* **2008**, *93*, 151904.
(66) Borca, C. N.; Xu, B.; Komesu, T.; Jeong, H. K.; Liu, M. T.; Liou, S. H. A. The Surface Phases of the $La_{0.65}Pb_{0.35}MnO_3$ Manganese Perovskite Surface. *Surf. Sci.* **2002**, *512*, L346−L.352.
(67) Jung, W.; Tuller, H. L. Investigation of Surface Sr Segregation in Model Thin Film Solid Oxide Fuel Cell Perovskite Electrodes. *Energy Environ. Sci.* **2011**, *5*, 5370−5378.
(68) Kubicek, M.; Limbeck, A.; Fromling, T.; Hutter, H.; Fleig, J. Relationship Between Cation Segregation and the Electrochemical Oxygen Reduction Kinetics of $La_{0.6}Sr_{0.4}CoO_{3-\delta}$ Thin Film Electrodes. *J. Electrochem. Soc.* **2011**, *158*, B727−B734.
(69) Cai, Z.; Kubicek, M.; Fleig, J.; Yildiz, B. Chemical Heterogeneities on $La_{0.6}Sr_{0.4}CoO_{3-\delta}$ Thin Films—Correlations to Cathode Surface Activity and Stability. *Chem. Mater.* **2012**, *24*, 1116−1127.
(70) Opitz, A. K.; Nenning, A.; Rameshan, C.; Rameshan, R.; Blume, R.; Hävecker, M.; Knop-Gericke, A.; Rupprechter, G.; Fleig, J.; Klötzer, B. Enhancing Electrochemical Water-Splitting Kinetics by Polarization-Driven Formation of Near-Surface Iron(0): An In Situ XPS Study on Perovskite-Type Electrodes. *Angew. Chem., Int. Ed.* **2015**, *54*, 2628−2632.
(71) Neagu, D.; Tsekouras, G.; Miller, D. N.; Menard, H.; Irvine, J. T. S. In Situ Growth of Nanoparticles Through Control of Non-Stoichiometry. *Nat. Chem.* **2013**, *5*, 916−923.
(72) Zimmermann, C.; Hayek, K. Computerunterstütztes Mikroreaktorsystem Zur Untersuchung Heterogen Katalysierter Gasreaktionen. *Chem. Eng. Technol.* **1991**, *63*, 68−71.
(73) Pecchini, M. P. U.S. Pat. 3,330,679, 1967.
(74) Opitz, A. K.; Hörlein, M. P.; Huber, T. M.; Fleig, J. Current-Voltage Characteristics of Platinum Model Electrodes on Yttria-Stabilized Zirconia. *J. Electrochem. Soc.* **2012**, *159*, B502−B513.
(75) Kogler, M.; Köck, E. M.; Bielz, T.; Pfaller, K.; Klötzer, B.; Schmidmair, D.; Perfler, L.; Penner, S. Hydrogen Surface Reactions and Adsorption Studied on $Y_2O_3$, YSZ, and $ZrO_2$. *J. Phys. Chem. C* **2014**, *118*, 8435−8444.
(76) Baumann, F. S.; Fleig, J.; Habermeier, H. U.; Maier, J. Impedance Spectroscopic Study on Well-Defined (La,Sr)(Co,Fe)$O_{3-d}$ Model Electrodes. *Solid State Ionics* **2006**, *177*, 1071−1081.
(77) Opitz, A. K.; Fleig, J. Investigation of $O_2$ Reduction on Pt/YSZ By Means of Thin Film Microelectrodes: The Geometry Dependence of the Electrode Impedance. *Solid State Ionics* **2010**, *181*, 684−693.
(78) Opitz, A. K.; Lutz, A.; Kubicek, M.; Kubel, F.; Hutter, H.; Fleig, J. Investigation of the Oxygen Exchange Mechanism on Pt|Yttria Stabilized Zirconia at Intermediate Temperatures: Surface Path Versus Bulk Path. *Electrochim. Acta* **2011**, *56*, 9727−9740.
(79) Kogler, S.; Nenning, A.; Rupp, G. M.; Opitz, A. K.; Fleig, J. Comparison of Electrochemical Properties of $La_{0.6}Sr_{0.4}FeO_{3-\delta}$ Thin Film Electrodes: Oxidizing vs. Reducing Conditions. *J. Electrochem. Soc.* **2015**, *162*, F317−F326.
(80) Orikasa, Y.; Nakao, T.; Oishi, M.; Ina, T.; Mineshige, A.; Amezawa, K.; Arai, H.; Ogumi, Z.; Uchimoto, Y. Local Structural Analysis for Oxide Ion Transport in $La_{0.6}Sr_{0.4}FeO_{3-\delta}$ Cathodes. *J. Mater. Chem.* **2011**, *21*, 14013−14019.
(81) Mizusaki, J.; Yoshihiro, M.; Yamauchi, S.; Fueki, K. Nonstoichiometry and Defect Structure of the Perovskite-Type Oxides $La_{1-x}Sr_xFeO_{3-\delta}$. *J. Solid Sate Chem.* **1985**, *58*, 257−266.
(82) Sogaard, M.; Vang Hendriksen, P.; Mogensen, M. Oxygen Nonstoichiometry and Transport Properties of Strontium Substituted Lanthanum Ferrite. *J. Solid Sate Chem.* **2007**, *180*, 1489−1503.
(83) Rothschild, A.; Menesklou, W.; Tuller, H. L.; Ivers-Tiffée, E. Electronic Structure, Defect Chemistry, and Transport Properties of $SrTi_{1-x}Fe_xO_3$ Solid Solutions. *Chem. Mater.* **2006**, *18*, 3651−3659.


DOI: 10.1021/acs.jpcc.5b02947
*J. Phys. Chem. C* 2015, 119, 11739−11753

(84) Bielz, T.; Lorenz, H.; Jochum, W.; Kaindl, R.; Klauser, F.; Klötzer, B.; Penner, S. Hydrogen on $In_2O_3$: Reducibility, Bonding, Defect Formation, and Reactivity. *J. Phys. Chem. C* **2010**, *114*, 9022−9029.
(85) Jochum, W.; Penner, S.; Föttinger, K.; Kramer, R.; Rupprechter, G.; Klötzer, B. Defect Formation and the Water-Gas Shift Reaction on $\beta$-$Ga_2O_3$. *J. Catal.* **2008**, *256*, 278−286.
(86) Tanaka, Y.; Utaka, T.; Kikuchi, I.; Sasaki, K.; Eguchi, K. CO Removal From Reformed Fuel over $Cu/ZnO/Al_2O_3$ Catalysts Prepared by Impregnation and Coprecipitation Methods. *Appl. Catal., A* **2003**, *238*, 11−18.
(87) Xue, E.; O'Keeffe, M.; Ross, J. R. H. Water-Gas Shift Conversion Using a Feed with a Low Steam to Carbon Monoxide Ratio and Containing Sulphur. *Catal. Today* **1996**, *30*, 107−118.
(88) Maroño, M.; Ruiz, E.; Sánchez, J. M.; Martos, C.; Dufour, J.; Ruiz, A. Performance of Fe-Cr Based WGS Catalysts Prepared by Co-Precipitation and Oxi-Precipitation Methods. *Int. J. Hydrogen Energy* **2009**, *34*, 8921−8928.
(89) Parkinson, G. S.; Novotný, Z.; Jacobson, P.; Schmid, M.; Diebold, U. Room Temperature Water Splitting at the Surface of Magnetite. *J. Am. Chem. Soc.* **2011**, *133*, 12650−12655.
(90) Adler, P.; Eriksson, S. Structural Properties, Mössbauer Spectra, and Magnetism of Perovskite-Type Oxides $SrFe_{1-x}Ti_xO_{3-y}$. *Z. Anorg. Allg. Chem.* **2000**, *626*, 118−124.
(91) Nielsen, W. G.; Skinner, J. G. Raman Spectrum of Strontium Titanate. *J. Chem. Phys.* **1968**, *48*, 2240.
(92) Petzelt, J.; Ostapchuk, T.; Gregora, I.; Kuzel, P.; Liu, J.; Shen, Z. Infrared and Raman Studies of the Dead Grain-Boundary Layers in $SrTiO_3$ Fine-Grain Ceramics. *J. Phys.: Condens. Matter* **2007**, *19*, 196222.
(93) Gosh, S.; Kamaraju, N.; Setu, M.; Fujimori, A.; Takeda, Y.; Ishiwata, S.; Kawasaki, S.; Azuma, M.; Takano, M.; Sood, A. K. Raman Scattering in $CaFeO_3$ and $La_{0.33}Sr_{0.67}FeO_3$ across the Charge-Disproportionation Phase Transition. *Phys. Rev. B* **2005**, *71*, 245110−1−245110−7.
(94) Lenser, C.; Kalinko, A.; Kuzmin, A.; Berzins, D.; Purans, J.; Szot, K.; Waser, R.; Dittmann, R. Spectroscopic Study of the Electric Field Induced Valence Change of Fe-Defect Centers in $SrTiO_3$. *Phys. Chem. Chem. Phys.* **2011**, *13*, 20779−20786.


DOI: 10.1021/acs.jpcc.5b02947
*J. Phys. Chem. C* 2015, 119, 11739−11753